

ISSN: 0256-307X

# 中国物理快报

# Chinese Physics Letters

Volume 33 Number 3 March 2016

A Series Journal of the Chinese Physical Society  
Distributed by IOP Publishing

Online: <http://iopscience.iop.org/0256-307X>  
<http://cpl.iphy.ac.cn>

CHINESE PHYSICAL SOCIETY  
**IOP** Publishing

JUST FOR AUTHORS  
— CHINESE PHYSICS LETTERS

## Microscopic Theory of the Thermodynamic Properties of $\text{Sr}_3\text{Ru}_2\text{O}_7$ \*

Wei-Cheng Lee(李伟正)<sup>1,2</sup>, Congjun Wu(吴从军)<sup>1\*\*</sup>

<sup>1</sup>Department of Physics, University of California, San Diego, California, 92093, USA

<sup>2</sup>Department of Physics, Applied Physics, and Astronomy, Binghamton University-State University of New York, Binghamton, USA

(Received 12 February 2016)

The thermodynamic properties of the bilayer ruthenate compound  $\text{Sr}_3\text{Ru}_2\text{O}_7$  at very low temperatures are investigated by using a tight-binding model yielding the realistic band structure combined with the on-site interactions treated at the mean-field level. We find that both the total density of states at the Fermi energy and the entropy exhibit a sudden increase near the critical magnetic field for the nematic phase, echoing the experimental findings. A new mechanism to explain the anisotropic transport properties is proposed based on scatterings at the anisotropic domain boundaries. Our results suggest that extra cares are necessary to isolate the contributions due to the quantum criticality from the band structure singularity in  $\text{Sr}_3\text{Ru}_2\text{O}_7$ .

PACS: 72.80.Ga, 73.20.-r, 71.10.Fd

DOI: 10.1088/0256-307X/33/3/037201

The bilayer ruthenate compound  $\text{Sr}_3\text{Ru}_2\text{O}_7$  has aroused considerable attentions with various interesting properties. It was first considered exhibiting a field-tuned quantum criticality of the metamagnetic transition.<sup>[1-3]</sup> Later, in the ultra-pure single crystal it has been found that the metamagnetic quantum critical point is intervened by the emergence of an unconventional anisotropic (nematic) electronic state,<sup>[4,5]</sup> stimulating considerable theoretical efforts.<sup>[6-18]</sup>  $\text{Sr}_3\text{Ru}_2\text{O}_7$  is a metallic itinerant system with the active  $t_{2g}$ -orbitals of the Ru sites in the bilayer  $\text{RuO}_2$  ( $ab$ ) planes. At very low temperatures ( $\sim 1$  K), it starts as a paramagnet at small magnetic fields. Further increasing field strength leads to two consecutive metamagnetic transitions at 7.8 and 8.1 Tesla if the field is perpendicular to the  $ab$ -plane. The nematic phase is observed between these two transitions, identified by the observation of anisotropic resistivity without noticeable lattice distortions.

This nematic phase in  $\text{Sr}_3\text{Ru}_2\text{O}_7$  can be understood as the consequence of a Fermi surface Pomeranchuk instability.<sup>[3]</sup> It is a mixture in both density and spin channels with the  $d$ -wave symmetry,<sup>[19]</sup> though its microscopic origin remains controversial. Different microscopic theories have been proposed based on the quasi-1D bands of  $d_{xz}$  and  $d_{yz}$ ,<sup>[14,15,18]</sup> and based on the 2d-band of  $d_{xy}$ .<sup>[8,9,16,17]</sup> In the theories of ours<sup>[14,18]</sup> and Raghu *et al.*,<sup>[15]</sup> the unconventional (nematic) magnetic ordering was interpreted as orbital ordering between the  $d_{xz}$  and  $d_{yz}$ -orbitals. In particular, in Ref. [18] a realistic tight-binding model is constructed taking into account the multi-orbital features, which reproduces accurately the results of the angle-resolved photon emission spec-

troscopy (ARPES)<sup>[20]</sup> and the quasiparticle interference in the spectroscopic imaging scanning tunneling microscopy (STM).<sup>[21]</sup>

The influence of quantum critical fluctuations in  $\text{Sr}_3\text{Ru}_2\text{O}_7$  seems to be novel as well. Rost *et al.*<sup>[22,23]</sup> measured the entropy and specific heat in ultra-pure samples and found divergences near the metamagnetic transitions in both quantities. Although it is a common feature in a quantum critical state that the specific heat diverges as  $C/T \sim [(B - B_c)/B_c]^{-\alpha}$  due to quantum fluctuations, the exponent of  $\alpha$  is fitted to be 1 instead of 1/3 as predicted by the celebrated Hertz-Millis theory.<sup>[24,25]</sup> The total density of states (DOS) measured by Iwaya *et al.*<sup>[26]</sup> using the STM showed that the DOS at the Fermi energy ( $\mathcal{D}(\epsilon_F)$ ) increases significantly under the magnetic field, but the DOS at higher and lower energy does not change accordingly. This indicates that the Zeeman energy does not simply cause a relative chemical potential shift to electrons with opposite spins (the DOS evolution with the external magnetic field will be discussed in Supplemental Material III B, i.e., SM III B). These findings have posted a challenge to understand the critical behavior in this material.

In this Letter, we show that the realistic band features of  $\text{Sr}_3\text{Ru}_2\text{O}_7$  make this material very sensitive to small energy scales. Parts of the Fermi surface are close to the van Hove singularities, and Fermi surface reconstructions in the external magnetic fields lead to a singular behavior in  $\mathcal{D}(\epsilon_F)$ . This results in the divergences observed in the experiments mentioned above. Because of the strong spin-orbit coupling and the unquenched orbital moments, the Zeeman energy tends to reconstruct the Fermi surfaces rather than just pro-

\*Supported by the NSF DMR-1410375 and AFOSR FA9550-14-1-0168, the President's Research Catalyst Award (No CA-15-327861) from the University of California Office of the President, and the CAS/SAFEA International Partnership Program for Creative Research Teams.

\*\*Corresponding author. Email: wucj@physics.ucsd.edu

© 2016 Chinese Physical Society and IOP Publishing Ltd

vides a relative chemical potential shift. Our results suggest that the influence of quantum critical fluctuations will be masked if  $\mathcal{D}(\epsilon_F)$  of the system exhibits a non-monotonic behavior, implying that a more careful analysis is required in order to distinguish the role of the quantum criticality in the bilayer  $\text{Sr}_3\text{Ru}_2\text{O}_7$ .

We employ the tight-binding model  $H_0$  for the band structure of  $\text{Sr}_3\text{Ru}_2\text{O}_7$  derived by two of us and Arovas in a previous work<sup>[18]</sup> as elaborated in SM I. It is featured by the  $t_{2g}$ -orbital structure (e.g.  $d_{xz}$ ,  $d_{yz}$ ,  $d_{xy}$ ), the bilayer splitting, the staggered distortion of the RuO octahedral, and spin-orbit coupling described by a few parameters as follows. The intra-layer hoppings include the longitudinal ( $t_1$ ) and transverse ( $t_2$ ) hoppings for the  $d_{xz}$  and  $d_{yz}$ -orbitals, the nearest neighbor ( $t_3$ ), the next nearest neighbor ( $t_4$ ), the next next nearest neighbor ( $t_5$ ) hoppings for the  $d_{xy}$ -orbital, and the next nearest neighbor ( $t_6$ ) hopping between  $d_{xz}$  and  $d_{yz}$ -orbitals. Here  $t_\perp$  is the longitudinal inter-layer hopping for the  $d_{xz}$  and  $d_{yz}$ -orbitals. The rotations of the RuO octahedra induce additional intra- ( $t_{\text{INT}}$ ) and inter-layer ( $t_{\text{INT}}^\perp$ ) hoppings between  $d_{xz}$  and  $d_{yz}$  orbitals. The onsite terms include the spin-orbit coupling  $\lambda\boldsymbol{\sigma} \cdot \mathbf{L}$ , the energy splitting  $V_{xy}$  of the  $d_{xz}$  and  $d_{yz}$  orbitals relative to the  $d_{xy}$ -orbital, and the chemical potential  $\mu$ . A typical Fermi surface configuration is plotted in Fig. 1 with the parameter values in the caption.

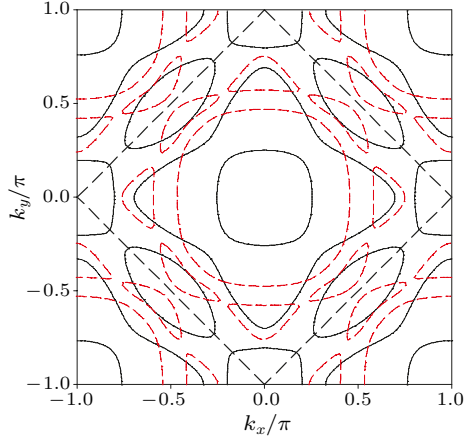


**Fig. 1.** The Fermi surfaces using the bilayer tight-binding model Eq. (1) in SM I with the parameters in units of  $t_1$  as:  $t_2 = 0.1t_1$ ,  $t_3 = t_1$ ,  $t_4 = 0.2t_1$ ,  $t_5 = -0.06t_1$ ,  $t_6 = 0.1t_1$ ,  $t_\perp = 0.6t_1$ ,  $t_{\text{INT}} = t_{\text{INT}}^\perp = 0.1t_1$ ,  $\lambda = 0.2t_1$ ,  $V_{xy} = 0.3t_1$ , and  $\mu = 0.94t_1$ . The thick dashed lines mark the boundary of the half Brillouin zone due to the unit cell doubling induced by the rotation of RuO octahedra. The Fermi surfaces of the bonding ( $k_z = 0$ ) and the anti-bonding bands ( $k_z = \pi$ ) are denoted by black solid and red dashed lines, respectively.

The Hubbard model contains the on-site intra and inter orbital interactions as

$$H_{\text{int}} = U \sum_{i,a,\alpha} \hat{n}_{ia\uparrow}^\alpha \hat{n}_{ia\downarrow}^\alpha + \frac{V}{2} \sum_{i,a,\alpha \neq \beta} \hat{n}_{ia}^\alpha \hat{n}_{ia}^\beta, \quad (1)$$

where the Greek index  $\alpha$  refers to the orbitals  $xz$ ,  $yz$

and  $xy$ ; the Latin index  $a$  refers to the upper and lower layers. The other two possible terms in the multi-band Hubbard interaction are the Hund rule coupling and pairing hopping terms, which do not change the qualitative physics and are neglected. We assume the external  $B$ -field lying in the  $xz$ -plane with an angle  $\theta$  tilted from the  $z$ -axis. The occupation and spin in each orbital and layer are defined as follows:  $n_a^\alpha \equiv \sum_s \langle d_{s,a}^{\alpha\dagger}(i) d_{s,a}^\alpha(i) \rangle$ ,  $S_{za}^\alpha \equiv \frac{1}{2} \sum_s s \langle d_{s,a}^{\alpha\dagger}(i) d_{s,a}^\alpha(i) \rangle$ ,  $S_{xa}^\alpha \equiv \frac{1}{2} \sum_s \langle d_{s,a}^{\alpha\dagger}(i) d_{s,a}^\alpha(i) \rangle$ , where  $s$  refers to spin index. The detailed mean-field theory solution for the Hamiltonian  $H_0 + H_{\text{int}}$  is presented in SM II, and order parameters are computed self-consistently. It was pointed out in Refs. [14,15] that the nematic phase can be identified as the orbital ordering between the  $d_{xz}$  and  $d_{yz}$ -orbitals. The nematic ( $\mathcal{N}$ ) and the magnetization ( $\mathcal{M}$ ) order parameters are defined as

$$\mathcal{N} = \sum_a (n_a^{yz} - n_a^{xz}), \quad \mathcal{M} = \sum_{a\alpha} S_a^\alpha. \quad (2)$$

Throughout this study, the interaction parameter values are taken as  $U/t_1 = V/t_1 = 3.6$ , such that no spontaneous magnetization occurs in the absence of the external magnetic field.

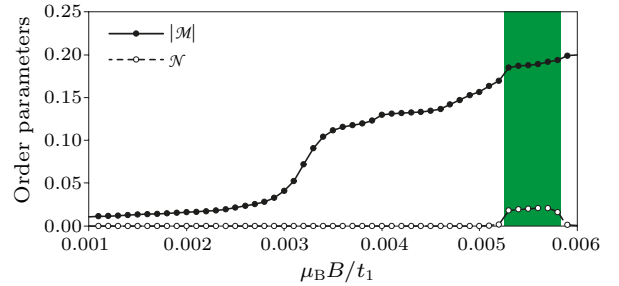


**Fig. 2.** The order parameters as a function of  $\mu_B B$  for  $\theta = 0$ . The nematic phase (in the green area) is bounded by two magnetization increases which correspond to metamagnetic transitions.

We present the mean-field results of low temperature thermodynamic properties at  $\mathbf{B} \parallel \hat{c}$ , i.e.,  $\theta = 0$ . Many experimentally observed results can be reproduced and understood by the singular behavior of  $\mathcal{D}(\epsilon_F)$  under the magnetic field. The order parameters  $|\mathcal{M}|$  and  $\mathcal{N}$  as functions of  $\mu_B B$  are shown in Fig. 2. There are three rapid increases in the magnetization, consistent with the experiment measurements of the real part of the very low frequency AC magnetic susceptibility at 7.5 T, 7.8 T and 8.1 T, respectively.<sup>[4]</sup> Experimentally, only the last two exhibit dissipative peaks in the imaginary part of the AC susceptibility, which characterize the first order metamagnetic transitions. The first jump measured is considered as a crossover. The nematic ordering develops in the area bounded by the last two magnetization jumps, reproducing the well-known phase diagram of the  $\text{Sr}_3\text{Ru}_2\text{O}_7$ .<sup>[4]</sup> In particular, if we adopt the results from LDA calculations<sup>[27,28]</sup> that  $t_1 \approx 300$  meV, we

can find that three jumps in the magnetization appear at  $B \approx 0.0032t_1/\mu_B$ ,  $0.0053t_1/\mu_B$ , and  $0.0059t_1/\mu_B \sim 15.7$  T, 26 T, and 29 T, which are within the same order to the experimental values. This is an improvement compared to the results in previous theory calculations.<sup>[8–11,15,16]</sup> in which the nematic ordering develops at much higher field strength  $\mu_B B/t_1 \approx 0.02$ .

The sensitivity of the nematic phase to the small energy scale like the Zeeman energy is because a part of the Fermi surfaces, mostly composed of quasi-1D bands, is approaching the van Hove singularities at  $(\pi, 0)$  and  $(0, \pi)$ . The evolution of the Fermi surface structures as increasing the  $B$ -field across the nematic phase boundaries is presented in detail in SM III A. When the system is in the nematic phase, the Fermi surfaces only have 2-fold symmetry as expected. Particularly, the nematic distortion is most prominent near  $(\pm\pi, 0)$  and  $(0, \pm\pi)$  whose Fermi surfaces are dominated by the quasi-1D bands, supporting the mechanism of orbital ordering in quasi-1D bands driven by the van Hove singularities.

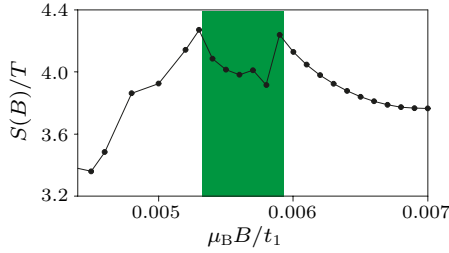


**Fig. 3.** (a) The entropy landscape represented by the quantity  $S(B)/T$  in units of  $k_B^2/t_1$  within the range of  $0.0045 \leq \mu_B B/t_1 \leq 0.007$ . A sudden increase near the nematic region (green area) is clearly seen.

One of the intriguing puzzles experimentally observed is the critical exponent of the divergence in entropy (as well as specific heat) when approaching the nematic region, or the quantum critical point. As mentioned in the introduction, the exponent does not match the Hertz-Millis theory based on the assumption of a constant DOS  $\mathcal{D}(\epsilon_F)$ . However,  $\text{Sr}_2\text{Ru}_3\text{O}_7$  has a complicated Fermi surface evolutions under the  $B$ -field, and is in the Fermi liquid state at low temperatures inferred from the temperature dependences of the resistivity. It is then worthy of studying first the contribution from the band structure to the entropy before considering the quantum fluctuations. The entropy per Ru atom can be evaluated by

$$S(B) = -\frac{k_B}{N} \sum_{\mathbf{k}} \sum_j [f(E_j(\mathbf{k})) \ln f(E_j(\mathbf{k})) + (1 - f(E_j(\mathbf{k}))) \ln(1 - f(E_j(\mathbf{k})))], \quad (3)$$

where  $f$  is the Fermi distribution function, and  $E_j(\mathbf{k})$  is the mean-field energy spectra of the  $j$ th band. In Fig. 3, we plot  $S(B)/T$  at a low temperature of  $1/(\beta t_1) = 0.002$  for the  $B$ -fields in the vicinity of

the nematic region.  $S(B)/T$  increases first, being suppressed, and then decreases, which is consistent with the experiment.<sup>[22]</sup> Since the nematic transition is driven by the sudden increase of  $\mathcal{D}(\epsilon_F)$ , the entropy should also be enhanced from outside towards the nematic region.

While it is generally expected that the quantum fluctuations near the critical point contribute additional entropy, our results demonstrate the singular behavior of  $\mathcal{D}(\epsilon_F)$  already produces diverging behavior in entropy under magnetic field at constant temperature, although the critical exponent  $\alpha$  is difficult to be extracted from the current theory. Similar argument has been proposed in a previous study,<sup>[23]</sup> in which the effect of a rigid band shift away from van Hove singularities in a perfect 1D band is discussed.

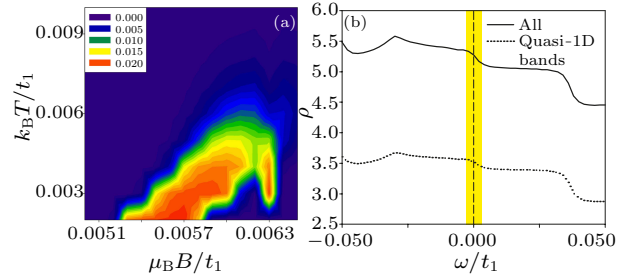


**Fig. 4.** (a) The  $T$ - $B$  phase diagram. Magnitudes of  $\mathcal{N}$  are represented by the color scales. The areas with light colors have large  $\mathcal{N}$ , defining the region for the nematic order. The re-entry of the nematic order at higher temperature is seen at fields between  $0.0058 < \mu_B B/t_1 < 0.0063$ . (b) The DOSs of the all bands (solid line) and quasi-1D bands (dashed line) at  $\mu_B B/t_1 = 0.006$ . The yellow areas refer to the energy window bounded by  $\pm k_B T/t_1$  with temperature  $k_B T/t_1 = 0.003$ . It can be seen that this thermal energy window covers a region in which the DOS increases abruptly, driving the nematic phase at finite temperature.

An intriguing experimental observation is the “muffin”-shaped phase boundary of the nematic phase in the  $T$ - $B$  phase diagram.<sup>[22]</sup> At field strengths slightly below 7.8 T and above 8.1 T the nematic phase appears at finite temperature but vanishes at zero temperature, to which we term as the “re-entry” behavior. It means that the entropy is actually higher inside the nematic phase than the adjacent normal phases. By inspecting Fig. 3 closer, it can be seen that the entropy drops as entering the nematic phase from the lower-field boundary but raises as entering from the upper-field boundary, thus the present theory has the “re-entry” at the upper-field boundary but not at the lower-field boundary, which is further confirmed by the temperature dependence of  $\mathcal{N}$  as a function of  $B$ -field shown in Fig. 4(a).

The re-entry behavior can be understood as follows. The mechanism for nematic ordering in  $\text{Sr}_3\text{Ru}_2\text{O}_7$  based on van Hove singularities is all about increasing  $\mathcal{D}(\epsilon_F)$  abruptly by driving the system closer to the van Hove singularities with the magnetic field. At the field strength slightly above the upper critical

field,  $\mathcal{D}(\epsilon_F)$  is large but still not enough for the occurrence of the nematic ordering. If the thermal energy is large enough to cover enough DOS within the thermal energy window  $\epsilon_F - k_B T < \epsilon_F < \epsilon_F + k_B T$  but still low enough so that the thermal fluctuations are small, the re-entry of the nematic phase at higher temperature is possible. As an illustration, Fig. 4(b) plots the DOS for  $\mu_B B/t_1 = 0.006$  at which the nematic ordering first occurs at  $k_B T/t_1 = 0.003$  in our calculation. It can be seen that the thermal energy window for  $k_B T/t_1 = 0.003$  (yellow areas) covers a region in which the DOS increases abruptly, consistent with the mechanism for the re-entry behavior discussed above.

Now let us consider the case of tilted magnetic field. Figure 5 presents the nematic order parameter  $\mathcal{N}$  as functions of  $\mu_B B$  and  $\theta$ . Since the in-plane component of the orbital Zeeman energy explicitly breaks the  $C_4$  symmetry down to the  $C_2$  symmetry,  $\mathcal{N}$  is non-zero as long as  $\theta \neq 0$ . Nevertheless, the experimentally observable nematic phase can still be identified by the jumps in  $\mathcal{N}$ . Our results show that the nematicity is strongly enhanced with increasing  $\theta$ , which is due to the orbital Zeeman energy. The anisotropic in-plane component of the orbital Zeeman energy term  $-\mu_B B \sum_{i,a} L_{x,ia} \sin \theta$  is clearly proportional to  $B$  and largest at  $\theta = 90^\circ$  (i.e.  $\hat{B} \parallel \hat{x}$ ), which induces the anisotropy of Fermi surface as explicitly shown in Fig. 3 in SM IV. Although such anisotropy in the band structure is not important at low field, it can be amplified by the effect of the interactions, driving the system more susceptible to the nematic phase as the critical points are approached. As a result, the portion of the nematic phase in the phase diagram is enlarged as  $\theta$  increases from  $0^\circ$  to  $90^\circ$  as seen in our calculations.

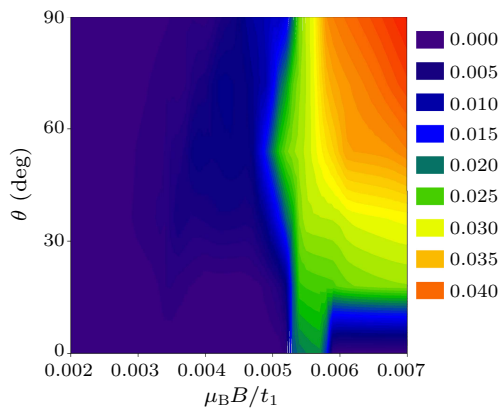


**Fig. 5.** The nematic order parameter  $\mathcal{N}$  as functions of  $\mu_B B$  and  $\theta$ . The magnitudes of  $\mathcal{N}$  are represented by the color scales.

However, experimentally the resistive anisotropy disappears quickly as the magnetic field is tilted away from the  $c$ -axis,<sup>[3,5,15]</sup> suggesting that the nematic ordering vanishes with the increase of the field angle  $\theta$ . This observation is seemingly in contradiction with our theory, but this disagreement can be reconciled

as follows. It has been argued that the resistivity measurement may not be a good indicator for the nematic phase in Ref. [15]: The nematic phase is mostly associated with states near the van Hove singularity where Fermi velocities are too small to contribute significantly to transport properties. The observed anisotropic resistivity is mostly likely due to the scatterings on nematic domains. The tilt of the magnetic field aligns domains, which makes the anisotropy explicit. However, if the domains are fully aligned, the resistivity measurement will become insensitive to the nematic phase due to the diminished scatterings between nematic domains even though the nematic order could be larger.

Our results have posted a possibility that the nematic order could occur in a larger range of the magnetic field for  $\mathbf{B} \parallel \hat{x}$  than for  $\mathbf{B} \parallel \hat{z}$ . Detection methods other than resistivity would be desirable. One feasible way is to measure the quasiparticle interference (QPI) in the spectroscopic imaging STM, which has been examined in detail in our previous work.<sup>[18]</sup> It has been predicted by us that if there is a nematic order, QPI spectra will manifest patterns breaking rotational symmetry. Another possible experiment is the nuclear quadrupole resonance (NQR) measurement, which has been widely used to reveal ordered states in high- $T_c$  cuprates<sup>[29–31]</sup> and recently the iron-pnictides.<sup>[32]</sup> This technique utilizes the feature that a nucleus with a nuclear spin  $I \geq 1$  has a non-zero electric quadrupole moment. Because the electric quadrupole moment creates energy splittings in the nuclear states as a electric field gradient is present, a phase transition could be inferred if substantial changes in the resonance peak are observed in the NQR measurement. In addition, since this is a local probe at the atomic level, it is highly sensitive to the local electronic change. Given that Ru atom has a nuclear spin of  $I = 5/2$ <sup>[33]</sup> and the orbital ordering in the quasi-1D bands significantly changes the charge distribution around the nuclei, a systematic NQR measurement as functions of magnetic field and field angle will reveal more conclusive information about nematicity.

One remaining puzzle on the transport anisotropy in the nematic phase is why the easy axis for the current flow is perpendicular to the in-plane component of the  $B$ -field.<sup>[5]</sup> In the following, we provide a natural explanation based on the anisotropic spatial extension of domain boundaries. Assuming the  $B$ -field lying in the  $xz$ -plane, the in-plane ( $xy$ ) orbital Zeeman energy reads  $H_{\text{in-plane}} = -\mu_B B \sin \theta \sum_{i,a} L_{x,ia}$ , which couples the  $d_{xy}$  and  $d_{xz}$ -orbitals and breaks the degeneracy between the  $d_{xz}$  and  $d_{yz}$ -orbitals. Since the  $d_{xy}$ -orbital has lower on-site energy due to the crystal field splitting than that of  $d_{xz}$ , the  $d_{xz}$ -orbital bands are pushed to higher energy than  $d_{yz}$ -orbital bands by this extra coupling. As a result, the nematic state with preferred  $d_{yz}$ -orbitals (i.e.,  $\mathcal{N} > 0$ ) has lower energy in the homogeneous system. At small



angles of  $\theta$ , domains with preferred  $d_{xz}$ -orbitals (i.e.  $\mathcal{N} \leq 0$ ) could form as depicted in Fig. 6(a) as metastable states, which occupy less volume than the majority domain of  $\mathcal{N} > 0$ .

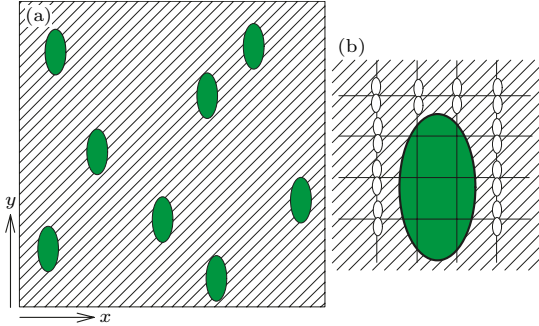


**Fig. 6.** Illustration of the energetically-favored domain structures as the in-plane magnetic field is along the  $\hat{x}$  axis. Orbital ordered phase with  $\mathcal{N} > 0$  are dominant (shaded areas) and high-energy domains with  $\mathcal{N} \leq 0$  (green ovals) coexist. (b) The domain walls extend longer in the  $\hat{y}$  direction because it costs less energies if less  $\hat{y}$ -than- $\hat{x}$  bonds are broken. The white oval represents the wavefunction of  $d_{yz}$  orbital on each site.

Let us consider the shape of the domain boundaries. Because of the quasi-1D features of the  $d_{xz}$  and  $d_{yz}$ -orbitals, the horizontal (vertical) domain wall breaks the bonds of the  $d_{yz}$  ( $d_{xz}$ )-orbital as depicted in Fig. 6(b), respectively. Since the  $d_{yz}$ -orbital is preferred by  $H_{\text{in-plane}}$ , the horizontal domain wall costs more energy. Consequently, the domain structure illustrated in Fig. 6(a) with longer vertical walls than the horizontal walls is energetically favored. Since the electrons suffer less domain scatterings hopping along the  $\hat{y}$ -axis in this domain structure, it becomes the easy axis for the current flow. At large values of  $\theta$ , higher energy domains are suppressed and eventually vanish, and thus the resistivity measurement becomes insensitive to the nematic phase because of vanishing of the domain scatterings.

In summary, we have shown that many important properties observed in the  $\text{Sr}_3\text{Ru}_2\text{O}_7$  could be qualitatively consistent with a realistic tight-binding model together with on-site interactions treated at mean-field level. The band structure is complicated by multibands, bilayer splitting, rotations of RuO octahedra, and the spin-orbit coupling, collectively leading to the high sensitivity to the small energy scales, which is the main cause of the singular behavior in the evolution of the Fermi surfaces under magnetic field. For the case of magnetic field parallel to the  $c$ -axis, the nematic order, which is interpreted as the orbital ordering in quasi-1D  $d_{yz}$  and  $d_{xz}$  bands, appears. The singular behavior in  $\mathcal{D}(\epsilon_F)$  also results in the diver-

gences in the entropy and specific heat landscapes. As the magnetic field is tilted away from the  $c$  axis ( $\theta \neq 0$ ), we find that the nematic region expands instead of shrinking as the resistivity measurement has indicated. To explain this discrepancy, we adopt the domain scattering argument.<sup>[15]</sup> Furthermore, we have given an explanation for another experimental puzzle that the easy axis for the current flow is always perpendicular to the in-plane magnetic field. Measurements like quasiparticle interference in the spectroscopic imaging STM and NQR which could detect the orbital ordering directly have been proposed.

We thank J. E. Hirsch and A. Mackenzie for valuable discussions.

## References

- [1] Grigera S A et al 2001 *Science* **294** 329
- [2] Perry R S et al 2001 *Phys. Rev. Lett.* **86** 2661
- [3] Grigera S A et al 2003 *Phys. Rev. B* **67** 214427
- [4] Grigera S A et al 2004 *Science* **306** 1154
- [5] Borzi R A et al 2007 *Science* **315** 214
- [6] Millis A J, Schofield A J, Lonzarich G G and Grigera S A 2002 *Phys. Rev. Lett.* **88** 217204
- [7] Green et al A G 2005 *Phys. Rev. Lett.* **95** 086402
- [8] Kee H Y and Kim Y B 2005 *Phys. Rev. B* **71** 184402
- [9] Yamase H and Katanin A 2007 *J. Phys. Soc. Jpn.* **76** 073706
- [10] Yamase H 2007 *Phys. Rev. B* **76** 155117
- [11] Puetter C, Doh H and Kee H Y 2007 *Phys. Rev. B* **76** 235112
- [12] Berridge A M, Green A G, Grigera S A and Simons B D 2009 *Phys. Rev. Lett.* **102** 136404
- [13] Berridge A M, Grigera S A, Simons B D and Green A G 2010 *Phys. Rev. B* **81** 054429
- [14] Lee W C and Wu C 2009 *Phys. Rev. B* **80** 104438
- [15] Raghu S et al 2009 *Phys. Rev. B* **79** 214402
- [16] Puetter C M, Rau J G and Kee H Y 2010 *Phys. Rev. B* **81** 081105
- [17] Fischer M H and Sigrist M 2010 *Phys. Rev. B* **81** 064435
- [18] Lee W C, Arovas D P and Wu C 2010 *Phys. Rev. B* **81** 184403
- [19] Wu C, Bergman D, Balents L and Das Sarma S 2007 *Phys. Rev. Lett.* **99** 70401
- [20] Tamai A et al 2008 *Phys. Rev. Lett.* **101** 026407
- [21] Lee J et al 2009 *Nat. Phys.* **5** 800
- [22] Rost A W et al 2009 *Science* **325** 1360
- [23] Rost A W et al 2010 *Phys. Status Solidi B* **247** 513
- [24] Hertz J A 1976 *Phys. Rev. B* **14** 1165
- [25] Millis A J 1993 *Phys. Rev. B* **48** 7183
- [26] Iwaya K et al 2007 *Phys. Rev. Lett.* **99** 057208
- [27] Liebsch A and Lichtenstein A 2000 *Phys. Rev. Lett.* **84** 1591
- [28] Eremin I, Manske D and Bennemann K 2002 *Phys. Rev. B* **65** 220502
- [29] Hammel P C et al 1998 *Phys. Rev. B* **57** R712
- [30] Teitelbaum G B, Büchner B and de Grönckel H 2000 *Phys. Rev. Lett.* **84** 2949
- [31] Singer P M, Hunt A W and Imai T 2002 *Phys. Rev. Lett.* **88** 047602
- [32] Lang G et al 2010 *Phys. Rev. Lett.* **104** 097001
- [33] Ishida K et al 1997 *Phys. Rev. B* **56** R505

## Supplemental Material for

# “Microscopic Theory of the Thermodynamic Properties of Sr<sub>3</sub>Ru<sub>2</sub>O<sub>7</sub>”

(See CHIN. PHYS. LETT. Vol. 33, No. 3 (2016) 037201)

Wei-Cheng Lee<sup>1,2,\*</sup> and Congjun Wu<sup>1,†</sup>

<sup>1</sup>*Department of Physics, University of California, San Diego, California, 92093, USA*

<sup>2</sup>*Department of Physics, Applied Physics, and Astronomy,  
Binghamton University-State University of New York, Binghamton, USA*

### I. THE TIGHT-BINDING MODEL

In this section, we explain the detailed band structure Sr<sub>3</sub>Ru<sub>2</sub>O<sub>7</sub>, which is complicated by the  $t_{2g}$ -orbital structure (e.g.  $d_{xz}, d_{yz}, d_{xy}$ ), the bilayer splitting, the staggered distortion of the RuO octahedra, and spin-orbit coupling. We have constructed a detailed tight-binding Hamiltonian which gives rise to band structures in agreement with the ARPES data in a previous work<sup>1</sup>. We found that a difference of the on-site potential between the two adjacent RuO layers,  $V_{\text{bias}}$ , should be added<sup>1</sup> in order to fit the shape of the Fermi surfaces observed in the ARPES experiments<sup>2</sup>. This term appears because ARPES is a surface probe and this bilayer symmetry breaking effect is important near the surface. Since we focus on the thermodynamic properties which are all bulk properties,  $V_{\text{bias}}$  is set to be zero in this paper. Below we will start from this model and refer readers to Ref. [1] for more detailed information.

The tight-binding band Hamiltonian  $H_0$  can be reduced to block forms classified by  $k_z = 0, \pi$  corresponding to bonding and anti-bonding bands with respect to layers as:

$$H_0 = h_0(k_z = 0) + h_0(k_z = \pi), \quad (1)$$

with  $h_0(k_z)$  defined as

$$h_0(k_z) = \sum_{\vec{k}}' \Phi_{\vec{k}, k_z, s}^\dagger \begin{pmatrix} \hat{h}_{0s}(\vec{k}, k_z) & \hat{g}^\dagger(\vec{k}, k_z) \\ \hat{g}(\vec{k}, k_z) & \hat{h}_{0s}(\vec{k} + \vec{Q}, k_z) \end{pmatrix} \Phi_{\vec{k}, k_z, s}, \quad (2)$$

where the spinor  $\Phi_{\vec{k}, k_z, s}^\dagger$  operator is defined as

$$\Phi_{\vec{k}, k_z, s}^\dagger = (d_{\vec{k}, s, k_z}^{yz \dagger}, d_{\vec{k}, s, k_z}^{xz \dagger}, d_{\vec{k}, -s, k_z}^{xy \dagger}, d_{\vec{k} + \vec{Q}, s, k_z}^{yz \dagger}, d_{\vec{k} + \vec{Q}, s, k_z}^{xz \dagger}, d_{\vec{k} + \vec{Q}, -s, k_z}^{xy \dagger}); \quad (3)$$

$d_{s, k_z}^\alpha(\vec{k})$  annihilates an electron with orbital  $\alpha$  and spin polarization  $s$  at momentum  $(\vec{k}, k_z)$ ;  $\vec{Q} = (\pi, \pi)$  is the nesting wavevector corresponding to unit cell doubling induced by the rotations of RuO octahedra;  $\sum_{\vec{k}}'$  means that only half of the Brillouin zone is summed. Please note the opposite spin configurations  $s$  and  $-s$  for the  $d_{xz}, d_{yz}$  and  $d_{xy}$ -orbitals in Eq. 3, which is convenient for adding spin-orbit coupling later.

The diagonal matrix kernels  $\hat{h}_{0s}$  in Eq. 2 are defined as

$$\hat{h}_{0s}(\vec{k}, k_z) = \hat{A}_s(\vec{k}) + \hat{B}_1 \cos k_z - \mu \hat{I}, \quad (4)$$

where

$$\hat{A}_s(\vec{k}) = \begin{pmatrix} \epsilon_{\vec{k}}^{yz} & \epsilon_{\vec{k}}^{\text{off}} + is\lambda & -s\lambda \\ \epsilon_{\vec{k}}^{\text{off}} - is\lambda & \epsilon_{\vec{k}}^{xz} & i\lambda \\ -s\lambda & -i\lambda & \epsilon_{\vec{k}}^{xy} \end{pmatrix}, \quad (5)$$

and

$$\hat{B}_1 = \begin{pmatrix} -t_\perp & 0 & 0 \\ 0 & -t_\perp & 0 \\ 0 & 0 & 0 \end{pmatrix}; \quad (6)$$

where  $t_\perp$  is the longitudinal inter-layer hopping for the  $d_{xz}$  and  $d_{yz}$  orbitals.  $\lambda$  is the spin-orbit coupling strength which comes from the on-site spin-orbit coupling term as  $H_{so} = \lambda \sum_i \vec{L}_i \cdot \vec{S}_i$ ;  $\mu$  is the chemical potential; the dispersions for the  $d_{yz}, d_{xz}$ , and  $d_{xy}$  bands in Eq. 5 are defined as

$$\begin{aligned} \epsilon_{\vec{k}}^{yz} &= -2t_2 \cos k_x - 2t_1 \cos k_y, \\ \epsilon_{\vec{k}}^{xz} &= -2t_1 \cos k_x - 2t_2 \cos k_y, \\ \epsilon_{\vec{k}}^{xy} &= -2t_3 (\cos k_x + \cos k_y) - 4t_4 \cos k_x \cos k_y \\ &\quad - 2t_5 (\cos 2k_x + \cos 2k_y) - V_{xy} \\ \epsilon_{\vec{k}}^{\text{off}} &= -4t_6 \sin k_x \sin k_y, \end{aligned} \quad (7)$$

which includes longitudinal ( $t_1$ ) and transverse ( $t_2$ ) hopping for the the  $d_{xz}$  and  $d_{yz}$  orbitals, respectively, as well as are nearest neighbor ( $t_3$ ), next-nearest neighbor ( $t_4$ ), and next-next-nearest neighbor ( $t_5$ ) hopping for the  $d_{xy}$  orbital. Following the previous LDA calculations<sup>3</sup>,  $V_{xy}$  is introduced to account for the splitting of the  $d_{yz}$  and  $d_{xz}$  states relative to the  $d_{xy}$  states. While symmetry forbids nearest-neighbor hopping between different  $t_{2g}$  orbitals in a perfect square lattice without the rotation of Ru octahedra, a term describing hopping between  $d_{xz}$  and  $d_{yz}$  orbitals on next-nearest neighbor sites ( $t_6$ ) is allowed and put into the tight-binding model.

The off-diagonal matrix kernel  $\hat{g}(\vec{k}, k_z)$  in Eq. 2 reads

$$\hat{g}(\vec{k}, k_z) = \hat{G}(\vec{k}) - 2\hat{B}_2 \cos k_z, \quad (8)$$

where

JUST FOR RESEARCH PURPOSES ONLY

$$\hat{B}_2 = \begin{pmatrix} 0 & t_{\text{INT}}^\perp & 0 \\ -t_{\text{INT}}^\perp & 0 & 0 \\ 0 & 0 & 0 \end{pmatrix}, \quad (9)$$

and

$$\hat{G}(\vec{k}) = \begin{pmatrix} 0 & -2t_{\text{INT}}\gamma(\vec{k}) & 0 \\ 2t_{\text{INT}}\gamma(\vec{k}) & 0 & 0 \\ 0 & 0 & 0 \end{pmatrix}, \quad (10)$$

with  $\gamma(\vec{k}) = \cos k_x + \cos k_y$ .  $t_{\text{INT}}$  and  $t_{\text{INT}}^\perp$  describe the intra- and inter-layer hopping between  $d_{xz}$  and  $d_{yz}$  induced by the rotations of RuO octahedra, providing the coupling between  $\vec{k}$  and  $\vec{k} + \vec{Q}$ .

When describing the Zeeman energy, we can choose the magnetic field  $\vec{B}$  to lie on the  $xz$  plane and define  $\theta$  as the angle between  $\vec{B}$  and the  $c$ -axis of the sample without loss of the generality. Consequently, the Zeeman term becomes:

$$\begin{aligned} H_{\text{Zeeman}} &= H_{\text{Zeeman}}^{\text{orbital}} + H_{\text{Zeeman}}^{\text{spin}}, \\ H_{\text{Zeeman}}^{\text{orbital}} &= -\mu_B B \sum_{i,a} (L_{z,ia} \cos \theta + L_{x,ia} \sin \theta), \\ H_{\text{Zeeman}}^{\text{spin}} &= -2\mu_B B \sum_{i,a,\alpha} (S_{z,ia}^\alpha \cos \theta + S_{x,ia}^\alpha \sin \theta), \end{aligned} \quad (11)$$

where  $a$  is the layer index,  $B = |\vec{B}|$ , and the matrices  $L_{x,z}$  can be found in Ref. [1].

For  $\theta \neq 0$ , the extra Zeeman terms from  $x$ -component of  $\vec{L}$  and  $\vec{S}$  couple  $\Phi_{\vec{k},k_z,\uparrow}^\dagger$  and  $\Phi_{\vec{k},k_z,\downarrow}^\dagger$ . Defining  $\phi_{\vec{k},k_z}^\dagger \equiv (\Phi_{\vec{k},k_z,\uparrow}^\dagger, \Phi_{\vec{k},k_z,\downarrow}^\dagger)$ , the Zeeman term can be written in the matrix form as:

$$H_{\text{Zeeman}} = \mu_B B \sum_{\vec{k}} \sum_{k_z} \phi_{\vec{k},k_z}^\dagger \hat{H}_Z(\theta) \phi_{\vec{k},k_z}, \quad (12)$$

where

$$\hat{H}_Z(\theta) = \begin{pmatrix} \hat{H}_Z^D(\theta, +) & 0 & \hat{H}_Z^{O\dagger}(\theta) & 0 \\ 0 & \hat{H}_Z^D(\theta, +) & 0 & \hat{H}_Z^{O\dagger}(\theta) \\ \hat{H}_Z^O(\theta) & 0 & \hat{H}_Z^D(\theta, -) & 0 \\ 0 & \hat{H}_Z^O(\theta) & 0 & \hat{H}_Z^D(\theta, -) \end{pmatrix}, \quad (13)$$

$$\hat{H}_Z^D(\theta, s) = \cos \theta \times \begin{pmatrix} -s & -i & 0 \\ i & -s & 0 \\ 0 & 0 & s \end{pmatrix}, \quad (14)$$

with  $s = \pm 1$  and

$$\hat{H}_Z^O(\theta) = \sin \theta \times \begin{pmatrix} -1 & 0 & 0 \\ 0 & -1 & -i \\ 0 & i & -1 \end{pmatrix}. \quad (15)$$

In realistic band structures measured by ARPES<sup>2</sup>, there exists an additional  $\delta$ -band arising from the  $d_{x^2-y^2}$ -orbital which is not covered by the current model. The particle filling in the  $t_{2g}$ -orbitals is not fixed. For the convenience of calculation, we fix the chemical potential  $\mu = 0.94t_1$  instead of fixing particle filling in the  $t_{2g}$ -orbitals while changing magnetic fields and orientations. The corresponding fillings inside the  $t_{2g}$ -orbitals per Ru atom varies within the range between 4.05 and 4.06 in Figs. 2, 4, 5 in the main text. This treatment does not change any essential qualitative physics.

## II. THE MEAN-FIELD THEORY

In this part, we present the process of mean-field theory solution.

The standard mean-field decomposition of  $H_{\text{int}}$  leads to

$$H_{\text{int}}^{MF} = \sum_{i,a,\alpha} \sum_s W_s^\alpha d_{s,a}^{\alpha\dagger}(i) d_{s,a}^\alpha(i) - U S_x^\alpha d_{s,a}^{\alpha\dagger}(i) d_{\bar{s},a}^\alpha(i), \quad (16)$$

where

$$W_s^\alpha = U \left( \frac{1}{2} n^\alpha - s S_z^\alpha \right) + V \sum_{\beta \neq \alpha} n^\beta, \quad (17)$$

with the assumptions of  $n_a^\alpha = n^\alpha$ ,  $S_{x,z}^\alpha = S_{x,z}^\alpha$ .

Since the order parameters  $\{n_a^\alpha\}$  are non-zero even without magnetic field, we require that the renormalized Fermi surface at zero field to be the one given in Fig. 1 in the main text. As a result, in addition to the optimized parameters obtained in our previous work<sup>1</sup>, we need to subtract the following term from Eq. 16:

$$H_{\text{shift}} = \sum_{i,a,\alpha} \sum_s W_s^\alpha(0) d_{s,a}^{\alpha\dagger}(i) d_{s,a}^\alpha(i), \quad (18)$$

where

$$W_s^\alpha(0) = \frac{1}{2} U n^\alpha(0) + V \sum_{\beta \neq \alpha} n^\beta(0), \quad (19)$$

and  $n^\alpha(0)$  is the occupation number in orbital  $\alpha$  corresponding to the Fermi surfaces shown in Fig. 1 in the main text. This is an effect of the renormalization of the chemical potential  $\mu$  and  $V_{xy}$  due to interactions. After putting all the pieces together, we finally arrive at the mean-field Hamiltonian as:

$$\begin{aligned} H^{MF} &= H_0 + H_{\text{int}}^{MF} - H_{\text{shift}} + H_{\text{Zeeman}} \\ &\equiv \sum_{\vec{k}} \sum_{k_z} \phi_{\vec{k},k_z}^\dagger H^{MF}(\vec{k}) \phi_{\vec{k},k_z}. \end{aligned} \quad (20)$$

The order parameters are computed self-consistently.



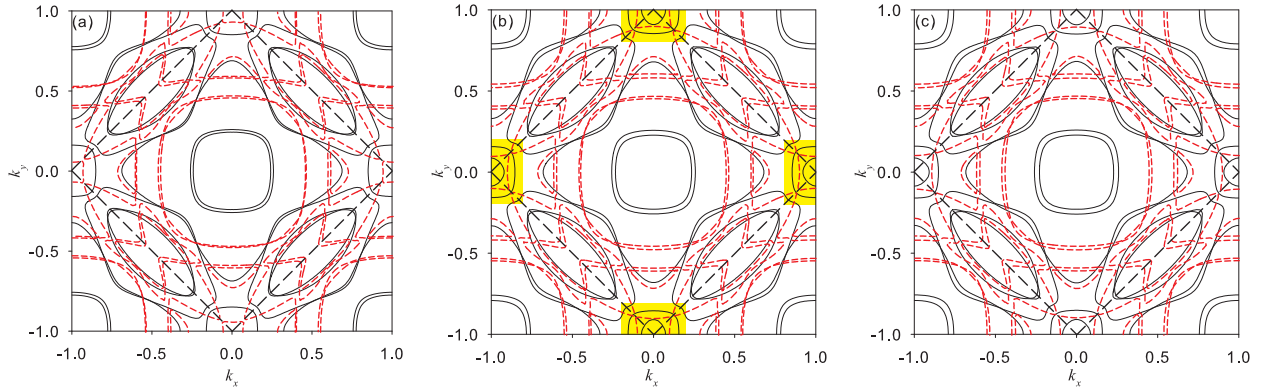


FIG. 1: Fermi surface evolution for the case of magnetic field parallel to  $c$  axis (a) before ( $\mu_B B = 0.0048t_1$ ) (b) inside ( $\mu_B B = 0.00544t_1$ ), and (c) after ( $\mu_B B = 0.006t_1$ ) the nematic phase. Significant changes in the Fermi surface topology under the magnetic field can be seen (see Fig. 1 in the main text for the Fermi surfaces at zero field). The nematic distortion is most obvious in the Fermi surfaces near  $(\pm\pi, 0)$  and  $(0, \pm\pi)$  as indicated by the yellow areas in (b). These parts of Fermi surfaces are composed mostly of quasi-1D bands, supporting the intimacy of nematic phase to the orbital ordering.

### III. THE CASE OF THE PERPENDICULAR MAGNETIC FIELD ( $\theta = 0$ )

In this section we present supplemental information for thermodynamic properties at low temperatures are calculated within the mean-field theory for the case of  $\vec{B} \parallel \hat{c}$ , *i.e.*,  $\theta = 0$ . They can be reasonably reproduced and understood by the singular behavior of  $\mathcal{D}(\epsilon_F)$  under the magnetic field.

#### A. Evolution of Fermi surface

We plot the part of Fermi surfaces mostly composed of quasi-1D bands as shown in the yellow areas in Fig. 1 (b), which is close to the van Hove singularities at  $(\pi, 0)$  and  $(0, \pi)$ . The evolution of the Fermi surface structures as increasing the B-field across the nematic phase boundaries is presented in Fig. 1 a (before), b (inside), and c (after) at  $\mu_B B/t_1 = 0.0048, 0.00544, 0.006$ , respectively. Before and after the nematic phases, the Fermi surfaces have the 4-fold rotational symmetry as exhibited in Fig. 1 (a) and (c), while the 4-fold symmetry is broken into 2-fold in the nematic phase.

It is worthy of mentioning that the onsite spin-orbit coupling  $H_{so} = \lambda \sum_i \vec{L}_i \cdot \vec{S}_i$  has important effects on the Fermi surface evolutions.  $H_{so}$  hybridizes the opposite spins between quasi-1D bands  $d_{yz, xz}$  and the 2-D band  $d_{xy}$ . As the spin Zeeman energy is present, the spin majority (minority) bands of  $d_{yz, xz}$  couples to the spin minority (majority) band of  $d_{xy}$ . Moreover, the orbital Zeeman energy provides more hybridizations between quasi-1D  $d_{xz, yz}$  bands. Combined with the above two effects, the addition of the spin and orbit Zeeman energies causes reconstruction of the Fermi surfaces rather than just chemical potential shifts. These results show

that the complexity and the sensitivity of the  $\text{Sr}_3\text{Ru}_2\text{O}_7$  band structure can be captured very well by our tight-binding model with a reasonable quantitative accuracy. In the following, the same model will be used to further investigate some novel physical properties observed in experiments.

#### B. Total density of states

Iwaya *et al.* has measured the STM tunneling differential conductance  $\frac{dI}{dV}$  in the  $B$ -field for  $\text{Sr}_3\text{Ru}_2\text{O}_7$ , which corresponds to measurement of the DOS. It has been observed that while DOS at higher and lower energy does not change, the DOS at the Fermi energy ( $\mathcal{D}(\epsilon_F)$ ) increase significantly under the application of the magnetic field, demonstrating the violation of the rigid band picture.

In our model the total DOS can be evaluated using:

$$\rho_{tot}(\omega) = \frac{1}{\pi N} \sum_{\vec{k}} \text{Tr} \text{Im} [\hat{G}^{MF}(\vec{k}, \omega)]$$

$$\hat{G}^{MF}(\vec{k}, \omega) \equiv (\omega + i\eta - H^{MF}(\vec{k}))^{-1} \quad (21)$$

where  $H^{MF}(\vec{k})$  is given in Eq. 20 with the self-consistent order parameters and  $N$  is the total number of sites in the bilayer square lattices.

The profiles of the total DOS at several different magnetic field strength are plotted in Fig. 2(a), and clearly a rigid band picture does not apply here.  $\mathcal{D}(\epsilon_F)$  ( $\rho_{tot}(\omega = 0)$  in the plot) increases significantly as the nematic phase is approached. This feature can also be directly understood by the picture of Fermi surface reconstruction, since the changes in the Fermi surface topology inevitably lead to the non-monotonic behavior in

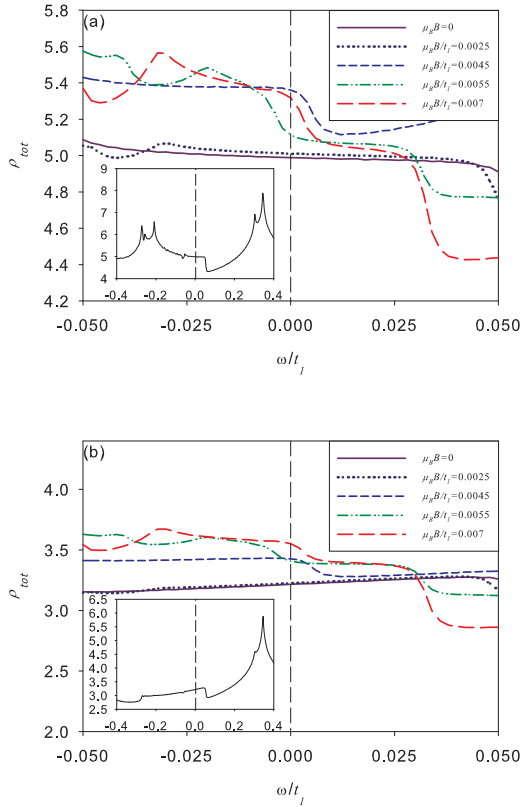


FIG. 2: (a) The total DOS  $\rho_{tot}(\omega)$  as a function of  $\mu_B B$ . The broadening factor  $\eta$  is set to be  $\eta = 0.002t_1$ .  $\rho_{tot}(\omega)$  does not follow the rigid band picture and  $\rho_{tot}(\omega = 0)$  has a sudden increase near the nematic region. Inset: the total DOS at zero field for a wider range of  $|\omega|/t_1 \leq 0.4$ . The peaks corresponding to van Hove singularities are near  $\omega/t_1 \approx -0.2$  and  $\omega/t_1 \approx 0.35$ . (b) The DOS of the quasi-1D bands. Inset: the DOS of quasi-1D bands at zero field for a wider range of  $|\omega|/t_1 \leq 0.4$ . Only the peak around  $\omega/t_1 \approx 0.35$  remains, meaning that this peak is due to the van Hove singularities in quasi-1D bands.

$\rho_{tot}(\omega = 0)$ . In particular, comparing Fig. 1 in the main text and Fig. 1 in this Supplemental Material, it is straightforward to see that more Fermi surfaces appear near the  $(\pm\pi, 0)$  and  $(0, \pm\pi)$  as the magnetic field increases. Since there are van Hove singularities near these four  $\vec{k}$  points,  $\rho_{tot}(\omega = 0)$  is expected to increase. As the magnetic field is increased further so that the van Hove singularities are all covered below the Fermi surfaces,  $\rho_{tot}(\omega = 0)$  starts to drop (not shown here).

At the first glance, the entropy measurement and our results of the total DOS seem to contradict with the STM measurement. While both the entropy measurement and our results develop a maximum around the nematic region in  $\mathcal{D}(\epsilon_F)$ , the STM measurement showed instead that  $\mathcal{D}(\epsilon_F)$  keeps increasing even after the nematic region is passed. To resolve this discrepancy, several realis-

tic features need to be considered before comparing our calculations with the STM results. Since the STM is a surface probe and the surface of the material is usually cleaved to have the oxygen atoms in the outermost layer, there is an oxygen atom lying above each uppermost Ru atom. Consequently, the tunneling matrix element will be mostly determined by the wavefunction overlaps between the  $p$ -orbitals of the oxygen atom and the  $d$ -orbitals of the Ru atom, resulting in a much smaller matrix element for  $d_{xy}$  orbital compared to  $d_{xz,yz}$  orbitals<sup>1</sup>. The minimal model to take this effect into account is to extract the DOS only from the quasi-1D orbitals, which is plotted in Fig. 2(b). Although the overall profile in Fig. 2(b) is not exactly the same as that in Ref. 4, which is attributed to more complicated momentum dependence of tunneling matrix elements<sup>5-7</sup> not considered here, it captures the increasing DOS with the magnetic field which is more consistent with Ref. 4.

The insets in Fig. 2 plot the total and quasi-1D band DOSs at zero field within a wider range of  $|\omega|/t_1 \leq 0.4$ . The peaks corresponding to the van Hove singularities reside at  $\omega/t_1 \approx -0.2$  and  $\omega/t_1 \approx 0.35$ , far away from the Fermi energy. The reason why the small energy scale like Zeeman energy ( $\sim 0.003t_1$ ) can push the system to get closer to the van Hove singularities at energies far away from the Fermi energy is the help of the metamagnetism. In the mean-field theory, the magnetization produces an effective chemical potential shift as  $sUS_z^\alpha$  for electrons at orbital  $\alpha$  and spin  $s$ . As a result, under the magnetic field the jump in the magnetization gives  $S_z^\alpha \sim 0.05$  within the range of experimental interests. This leads to the effective chemical potential shift about  $\pm 0.18t_1$  for  $U = 3.6t_1$ , which is large enough to push the system closer to the van Hove singularities. This renormalization of the chemical potential by the interaction is also part of the cause for the violation of the rigid band picture.

#### IV. THE CASE OF THE TILTED MAGNETIC FIELDS ( $\theta \neq 0$ )

We present the Fermi surface configuration in the presence of tilted magnetic field. The Fermi surfaces without any interaction for  $\vec{B} \parallel \hat{x}$  with strength  $\mu_B |\vec{B}| = 0.1t_1$  is plotted in Fig. 3, and an anisotropy can be seen. Although such anisotropy in the band structure is not important at low field, it can be amplified by the effect of the interactions, driving the system more susceptible to the nematic phase as the critical points is approached. As a result, the portion of the nematic phase in the phase diagram is enlarged as  $\theta$  increases from  $0^\circ$  to  $90^\circ$  as seen in our calculations.

#### V. SUMMARY AND MORE DISCUSSIONS

The failure of a rigid band picture is essentially a consequence of the interplay between spin-orbit coupling and

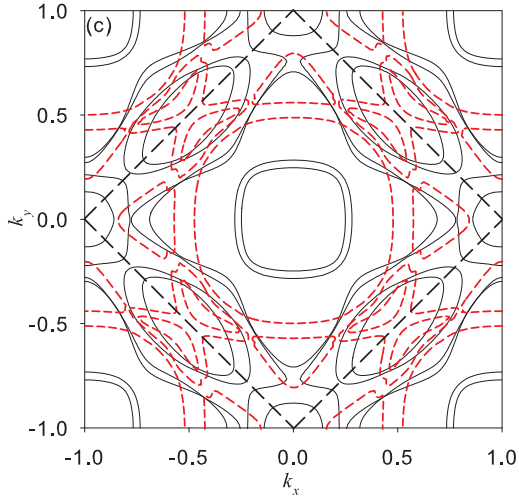


FIG. 3: The non-interacting Fermi surfaces for  $\vec{B} \parallel \hat{x}$  and  $\mu_B B = 0.1t_1$ . The anisotropy in Fermi surfaces is already visible, especially for the areas near  $(\pm\pi, 0)$  and  $(0, \pm\pi)$ .

the Zeeman energy, despite the strong correlation effect could also result in the violation of the rigid band shift upon doping<sup>8</sup>. Because the spin-orbit coupling hybridizes the quasi-1D bands and 2-D bands with *opposite* spins, the Zeeman energy naturally induces the reconstruction of the Fermi surfaces instead of just rigid chemical potential shifts. This singular behavior in  $\mathcal{D}(\epsilon_F)$  also results in the divergences in the entropy and specific heat landscapes, since at very low temperature both quantities are approximately proportional to  $\mathcal{D}(\epsilon_F)$ . Because the divergence observed by Rost *et. al.*<sup>9</sup> start approximately at 6-7 Tesla which is not very close to the quantum critical point residing about 8 Tesla, a direct application of the quantum critical scaling seems to be inappropriate. The explanation of the critical exponent associated with this divergence could not be complete without taking the band structure singularity into account in this particular material<sup>10</sup>.

As the magnetic field is tilted away from the  $c$  axis ( $\theta \neq 0$ ), we find that nematic region expands instead of shrinking as the resistivity measurement has indicated. From the theoretical viewpoints, the tilt of the magnetic field induces an extra in-plane component of the orbital Zeeman energy which explicitly breaks the  $C_4$  symmetry down to the  $C_2$  symmetry. As argued above that this system is very sensitive to small energy scale, the effect of this extra Zeeman energy is not important at low field but could amplify the effect of interaction to drive the system toward nematicity as the quantum critical point is approached. As a result, the nematic phase is more favored and stable in the presence of the in-plane magnetic field and it requires another Fermi surface reconstruc-

tion at even higher magnetic field in order to weaken the nematic phase by reduced  $\mathcal{D}(\epsilon_F)$ .

To explain this discrepancy between our theory and the resistivity measurement, we adopt the domain scattering argument proposed by Raghu *et. al.*<sup>11</sup>. Furthermore, we have given an explanation for another experimental puzzle that the easy axis for the current flow is always perpendicular to the in-plane magnetic field. Measurements like quasiparticle interference in the spectroscopic imaging STM and NQR which could detect the orbital ordering directly have been proposed to be more reliable probes for the nematicity in this material than the resistivity measurement.

Finally we would like to comment on limitation of the present theory. Although we have found the 're-entry' behavior of the nematic phase, i.e., the appearance of the nematic phase only at the finite temperature but not at the zero temperature, near the upper-field boundary, the experiments showed this behavior near both upper- and lower- field boundary. In our calculations, the re-entry behavior is due to the increase of the density of states within the narrow energy window around the Fermi energy opened by thermal energy, but we do not reject other schemes for the re-entry behavior. One possible scheme is an analogue of ferromagnetism without exchange splitting proposed by Hirsch<sup>12</sup>. He showed that the nearest neighbor interactions could result in a spin-dependent renormalization on the bandwidth (equivalently, the effective mass). As a result, the filling for different spin bands can be different because of the unequal effective masses, leading to the ferromagnetism even without the exchange splitting as in the Stoner model.

In Hirsch's original paper, the re-entry of the ferromagnetism at higher temperature was found. Since we only considered the on-site interactions in our model, such an effect is beyond the scope of the current theory. It is possible that after including the nearest neighbor interaction, the renormalizations of the bandwidths have novel temperature-dependences, leading to a phase diagram better consistent with the experiments. If this is the correct scheme, the re-entry of the nematic states should be accompanied by a change in the kinetic energy due to the effective mass renormalization, which could be examined by the sum rules for the optical properties<sup>12-16</sup>.

Another possible scheme for the re-entry behavior is the quantum critical fluctuations. It is well-known that the influences of the critical fluctuations extend from the quantum critical point to finite temperature in a V-shape region in the phase diagram. Moreover, the critical fluctuations in this material contain not only the ferromagnetic but also the nematic ones. As a result, it is not surprising that the competition between these two types of critical fluctuations leads to a intriguing phase diagram at the finite temperature, and the study toward this direction is currently in progress.

---

\* Electronic address: [leewc@physics.ucsd.edu](mailto:leewc@physics.ucsd.edu)

† Electronic address: [wucj@physics.ucsd.edu](mailto:wucj@physics.ucsd.edu)

<sup>1</sup> W.-C. Lee, D. P. Arovas, and C. Wu, *Phys. Rev. B* **81**, 184403 (2010).

<sup>2</sup> A. Tamai *et al.*, *Phys. Rev. Lett.* **101**, 026407 (2008).

<sup>3</sup> D. Singh and I. Mazin, *Phys. Rev. B* **63**, 165101 (2001).

<sup>4</sup> K. Iwaya *et al.*, *Phys. Rev. Lett.* **99**, 057208 (2007).

<sup>5</sup> J. Tersoff and D. Hamann, *Phys. Rev. Lett.* **50**, 1998 (1983).

<sup>6</sup> Y. Zhang *et al.*, *Nat. Phys.* **4**, 627 (2008).

<sup>7</sup> W.-C. Lee and C. Wu, *Phys. Rev. Lett.* **103**, 176101 (2009).

<sup>8</sup> J. Farrell *et al.*, *Phys. Rev. B* **78**, 180409 (2008).

<sup>9</sup> A. W. Rost *et al.*, *Science* **325**, 1360 (2009).

<sup>10</sup> J. Lee *et al.*, *Nat. Phys.* **5**, 800 (2009).

<sup>11</sup> S. Raghu *et al.*, *Phys. Rev. B* **79**, 214402 (2009).

<sup>12</sup> J. E. Hirsch, *Phys. Rev. B* **59**, 6256 (1999).

<sup>13</sup> Y. Okimoto *et al.*, *Phys. Rev. Lett.* **75**, 109 (1995).

<sup>14</sup> Y. Okimoto *et al.*, *Phys. Rev. B* **55**, 4206 (1997).

<sup>15</sup> D. N. Basov and T. Timusk, *Rev. Mod. Phys.* **77**, 721 (2005).

<sup>16</sup> A. D. LaForge *et al.*, *Phys. Rev. Lett.* **101**, 097008 (2008).

JUST FOR AUTHORS  
— CHINESE PHYSICS LETTERS

# Chinese Physics Letters

Volume 33

Number 3

March 2016

## GENERAL

- 030301 Schrödinger Equation of a Particle on a Rotating Curved Surface**  
Long Du, Yong-Long Wang, Guo-Hua Liang, Guang-Zhen Kang, Hong-Shi Zong
- 030302 Biased Random Number Generator Based on Bell's Theorem**  
Yong-Gang Tan, Yao-Hua Hu, Hai-Feng Yang
- 030303 Post-processing Free Quantum Random Number Generator Based on Avalanche Photodiode Array**  
Yang Li, Sheng-Kai Liao, Fu-Tian Liang, Qi Shen, Hao Liang, Cheng-Zhi Peng
- 030401 Generalised Error Functions from the Kerr Metric**  
Wen-Lin Tang, Zi-Ren Luo, Yun-Kau Lau

## THE PHYSICS OF ELEMENTARY PARTICLES AND FIELDS

- 031301 Chargino Production via  $Z^0$ -Boson Decay in a Strong Electromagnetic Field**  
Alexander Kurilin

## NUCLEAR PHYSICS

- 032101 The Brueckner–Hartree–Fock Equation of State for Nuclear Matter and Neutron Skin**  
Qing-Yang Bu, Zeng-Hua Li, Hans-Josef Schulze

## ATOMIC AND MOLECULAR PHYSICS

- 033201 Stark-Broadened Profiles of the Spectral Line  $P_\alpha$  in He II Ions**  
Bin Duan, Muhammad Abbas Bari, Ze-Qing Wu, Jun Yan, Jian-Guo Wang
- 033401 Magnetic-Field Dependence of Raman Coupling Strength in Ultracold  $^{40}\text{K}$  Atomic Fermi Gas**  
Liang-Hui Huang, Peng-Jun Wang, Zeng-Ming Meng, Peng Peng, Liang-Chao Chen, Dong-Hao Li, Jing Zhang

## FUNDAMENTAL AREAS OF PHENOMENOLOGY (INCLUDING APPLICATIONS)

- 034201 Generation of Q-Switched Mode-Locked Erbium-Doped Fiber Laser Operating in Dark Regime**  
Zian Cheak Tiu, Arman Zarei, Harith Ahmad, Sulaiman Wadi Harun
- 034202 Tunable and Switchable Narrow Bandwidth Semiconductor-Saturable Absorber Mirror Mode-Locked Yb-Doped Fiber Laser Delivering Different Pulse Widths**  
Zhao-Kun Wang, Feng Zou, Zi-Wei Wang, Song-Tao Du, Jun Zhou
- 034203 Ghost Imaging with High Visibility Using Classical Light Source**  
Yu Si, Ling-Jun Kong, Yong-Nan Li, Cheng-Hou Tu, Hui-Tian Wang
- 034204 Broad-Band All-Optical Wavelength Conversion of Differential Phase-Shift Keyed Signal Using an SOA-Based Nonlinear Polarization Switch**  
Ya-Ya Mao, Xin-Zhi Sheng, Chong-Qing Wu, Kuang-Lu Yu
- 034205 Transverse Localization of Light in 1D Self-Focusing Parity-Time-Symmetric Optical Lattices**  
Xing Wei, Bin Chen, Chun-Fang Wang
- 034301 Bayesian Tracking in an Uncertain Shallow Water Environment**  
Qian-Qian Li

JUST FOR AUTHORS  
— CHINESE PHYSICS LETTERS



## PHYSICS OF GASES, PLASMAS, AND ELECTRIC DISCHARGES

- 035201 **Electron-Cyclotron Laser Using Free-Electron Two-Quantum Stark Radiation in a Strong Uniform Axial Magnetic Field and an Alternating Axial Electric Field in a Voltage-Supplied Pill-Box Cavity**  
S. H. Kim
- 035202 **Using Target Ablation for Ion Beam Quality Improvement**  
Shuan Zhao, Chen Lin, Jia-Er Chen, Wen-Jun Ma, Jun-Jie Wang, Xue-Qing Yan
- 035203 **Time-Resolved Transmission Measurements of Warm Dense Iron Plasma**  
Bo Qing, Yang Zhao, Min-Xi Wei, Hang Li, Gang Xiong, Min Lv, Zhi-Min Hu, Ji-Yan Zhang, Jia-Min Yang

## CONDENSED MATTER: STRUCTURE, MECHANICAL AND THERMAL PROPERTIES

- 036101 **Bubble Generation in Germanate Glass Induced by Femtosecond Laser**  
Jue-Chen Wang, Qiang-Bing Guo, Xiao-Feng Liu, Ye Dai, Zhi-Yu Wang, Jian-Rong Qiu
- 036201 **Spall Strength of Resistance Spot Weld for QP Steel**  
Chun-Lei Fan, Bo-Han Ma, Da-Nian Chen, Huan-Ran Wang, Dong-Fang Ma
- 036202 **Ground-State Structure and Physical Properties of NB<sub>2</sub> Predicted from First Principles**  
Jing-He Wu, Chang-Xin Liu

## CONDENSED MATTER: ELECTRONIC STRUCTURE, ELECTRICAL, MAGNETIC, AND OPTICAL PROPERTIES

- 037101 **Splitting Phenomenon Induced by Magnetic Field in Metallic Carbon Nanotubes**  
Gui-Li Yu, Yong-Lei Jia, Gang Tang
- 037201 **Microscopic Theory of the Thermodynamic Properties of Sr<sub>3</sub>Ru<sub>2</sub>O<sub>7</sub>**  
Wei-Cheng Lee, Congjun Wu
- 037301 **Light-Emitting Diodes Based on All-Quantum-Dot Multilayer Films and the Influence of Various Hole-Transporting Layers on the Performance**  
Hui-Li Yin, Su-Ling Zhao, Zheng Xu, Li-Zhi Sun
- 037302 **Tunneling Negative Magnetoresistance via  $\delta$  Doping in a Graphene-Based Magnetic Tunnel Junction**  
Jian-Hui Yuan, Ni Chen, Hua Mo, Yan Zhang, Zhi-Hai Zhang
- 037303 **Spin Caloritronic Transport of 1,3,5-Triphenylverdazyl Radical**  
Qiu-Hua Wu, Peng Zhao, De-Sheng Liu
- 037401 **Single Crystal Growth and Physical Property Characterization of Non-centrosymmetric Superconductor PbTaSe<sub>2</sub>**  
Yu-Jia Long, Ling-Xiao Zhao, Pei-Pei Wang, Huai-Xin Yang, Jian-Qi Li, Hai Zi, Zhi-An Ren, Cong Ren, Gen-Fu Chen
- 037501 **Zero-Magnetic-Field Oscillation of Spin Transfer Nano-Oscillator with a Second-Order-Perpendicular-Anisotropy Free Layer**  
Yuan-Yuan Guo, Fei-Fei Zhao, Hai-Bin Xue, Zhe-Jie Liu
- 037502 **A Single-Crystal Neutron Diffraction Study on Magnetic Structure of the Quasi-One-Dimensional Antiferromagnet SrCo<sub>2</sub>V<sub>2</sub>O<sub>8</sub>**  
Juan-Juan Liu, Jin-Chen Wang, Wei Luo, Jie-Ming Sheng, Zhang-Zhen He, S. A. Danilkin, Wei Bao
- 037801 **Improvement of the Conductivity of Silver Nanowire Film by Adding Silver Nano-Particles**  
Yi Shen, Ruo-He Yao

## CROSS-DISCIPLINARY PHYSICS AND RELATED AREAS OF SCIENCE AND TECHNOLOGY

- 038101 **Characterization of Elastic Modulus of Granular Materials in a New Designed Uniaxial Oedometric System**  
Qin-Wei Ma, Yahya Sandali, Rui-Nan Zhang, Fang-Yuan Ma, Hong-Tao Wang, Shao-Peng Ma, Qing-Fan Shi

- 038201 Comparisons of Criteria for Analyzing the Dynamical Association of Solutes in Aqueous Solutions**  
Liang Zhao, Yu-Song Tu, Chun-Lei Wang, Hai-Ping Fang
- 038501 Highly Efficient Greenish-Yellow Phosphorescent Organic Light-Emitting Diodes Based on a Novel 2,3-Diphenylimidazo[1,2-a]Pyridine Iridium(III) Complex**  
Jun Sun, Min Xi, Zi-Sheng Su, Hai-Xiao He, Mi Tian, Hong-Yan Li, Hong-Ke Zhang, Tao Mao, Yu-Xiang Zhang
- 038502 Electrical Instability of Amorphous-Indium-Gallium-Zinc-Oxide Thin-Film Transistors under Ultraviolet Illumination**  
Lan-Feng Tang, Hai Lu, Fang-Fang Ren, Dong Zhou, Rong Zhang, You-Dou Zheng, Xiao-Ming Huang,
- 038503 Current Controlled Relaxation Oscillations in  $\text{Ge}_2\text{Sb}_2\text{Te}_5$ -Based Phase Change Memory Devices**  
Yao-Yao Lu, Dao-Lin Cai, Yi-Feng Chen, Yue-Qing Wang, Hong-Yang Wei, Ru-Ru Huo, Zhi-Tang Song
- 038801 Comprehensive Study of  $\text{SF}_6/\text{O}_2$  Plasma Etching for Mc-Silicon Solar Cells**  
Tao Li, Chun-Lan Zhou, Wen-Jing Wang
- 038901 Fractal Analysis of Mobile Social Networks**  
Wei Zheng, Qian Pan, Chen Sun, Yu-Fan Deng, Xiao-Kang Zhao, Zhao Kang

### **GEOFYSICS, ASTRONOMY, AND ASTROPHYSICS**

- 039801 Consistency Conditions and Constraints on Generalized  $f(R)$  Gravity with Arbitrary Geometry-Matter Coupling**  
Si-Yu Wu, Ya-Bo Wu, Yue-Yue Zhao, Xue Zhang, Cheng-Yuan Zhang, Bo-Hai Chen

**JUST FOR AUTHORS**  
— CHINESE PHYSICS LETTERS